HEALTH AND MEDICINE

Biomaterials with structural hierarchy and controlled 3D nanotopography guide endogenous bone regeneration

Shixuan Chen[1], Hongjun Wang[1], Valerio Luca Mainardi[2,3], Giuseppe Talò[4], Alec McCarthy[1], Johnson V. John[1], Matthew J. Teusink[5], Liu Hong[6], Jingwei Xie[1,7]*

Biomaterials without exogenous cells or therapeutic agents often fail to achieve rapid endogenous bone regeneration with high quality. Here, we reported a class of three-dimensional (3D) nanofiber scaffolds with hierarchical structure and controlled alignment for effective endogenous cranial bone regeneration. 3D scaffolds consisting of radially aligned nanofibers guided and promoted the migration of bone marrow stem cells from the surrounding region to the center in vitro. These scaffolds showed the highest new bone volume, surface coverage, and mineral density among the tested groups in vivo. The regenerated bone exhibited a radially aligned fashion, closely recapitulating the scaffold's architecture. The organic phase in regenerated bone showed an aligned, layered, and densely packed structure, while the inorganic mineral phase showed a uniform distribution with smaller pore size and an even distribution of stress upon the simulated compression. We expect that this study will inspire the design of next-generation biomaterials for effective endogenous bone regeneration with desired quality.

INTRODUCTION

Large calvarial bone defects often occur because of congenital anomalies, trauma, stroke, aneurysms, and cancer (*1*, *2*). Although application of free vascularized bone grafts from distant sites may represent the most reliable procedure, it is associated with issues including the size and shape mismatch, bone resorption, and secondary morbidity (*3*). Regenerative medicine approaches involving delivery of cells to defect sites have generated disappointing and inconsistent results (*4*). While recombinant human bone morphogenetic protein-2 (BMP-2) is currently approved for the bone repair and regeneration, this therapeutic is associated with notable side effects (e.g., ectopic bone formation and bone resorption) and high cost (*5*, *6*). Biomaterials including bioglass, titanium, poly(etheretherketone), poly(methyl methacrylate), and hydroxyapatite have emerged for cranioplasty (*7*). However, none of these conventional materials are ideal likely due to their nonoptimal structures (e.g., small pore size, low porosity, and lack of nanotopographical cues). In addition, most cranioplasty materials are nonbiodegradable, resulting in restricted growth and deformation of the skull in pediatric patients (*8*). Therefore, there is a great demand for development of inexpensive and resorbable graft without incorporation of living cells and therapeutics, eliminating the need for a second surgical site and substantial drawbacks associated with the use of allografts, current cranioplasty materials, and growth factors.

New biomaterials that can promote tissue repair and regeneration on their own without the need for cells or other therapeutics have emerged as a potentially powerful paradigm for regenerative medicine (*4*). Topographical cues rendered by biomaterials have been extensively investigated to guide cell response including adhesion, spreading, alignment, migration, and gene expression (*9*, *10*). In particular, aligned topographical cues have been incorporated into two-dimensional (2D) substrates created by electron beam lithography, colloidal lithography, photolithography, laser lithography, and injection molding for in vitro regulation of cellular response (*11*–*13*). Although these studies may provide useful information on the design of biomaterials for regulating cell behavior, the 2D grooved/patterned substrates are not physiologically relevant, lacking biomimetic property and capacity in forming aligned nanotopography in 3D (*14*). Besides, the technical challenge still remains to incorporate 3D biomimicking, aligned nanotopographical cues into hierarchically structured biomaterials. To overcome these problems, we reported a class of biomaterials made of polycaprolactone (PCL) electrospun nanofibers with structural hierarchy and predesigned 3D aligned nanotopography and their evaluations in vitro and in vivo in terms of cell response and bone regeneration efficacy. We chose PCL as the raw material for nanofiber assemblies in that it has been used in the U.S. Food and Drug Administration (FDA)–approved implants and sutures (e.g., Osteoplug, Osteomesh, and Monoderm) and is fully resorbable in 18 to 24 months (*15*, *16*). The gradual resorption profile makes it a predictable material for matching the natural stage of bone healing where cancellous bone tissues completely form in about 6 months followed by remodeling phase to cortical bones over 2 to 3 years (*17*). Similarly, we chose gelatin for coating nanofiber assemblies as it has been used in FDA-approved medical devices (e.g., Gelfoam) (*18*). We hypothesized that the 3D scaffolds consisting of radially aligned nanofibers (RAS) and vertically aligned nanofibers (VAS) can guide and promote cell migration either from the surrounding to the center or from the bottom to the top, resulting in rapid bone regeneration after implantation to critical-sized calvarial bone defects in rats. Our approach shows great promise for the development of next generation of cell- and therapeutic agent–free biomaterials for effective endogenous bone repair.

[1]Department of Surgery-Transplant and Mary & Dick Holland Regenerative Medicine Program, University of Nebraska Medical Center, Omaha, NE 68198, USA. [2]Regenerative Medicine Technologies Lab, Ente Ospedaliero Cantonale (EOC), via Tesserete 46, 6900, Lugano, Switzerland. [3]Laboratory of Biological Structures Mechanics (LaBS), Department of Chemistry, Material and Chemical Engineering "Giulio Natta", Politecnico di Milano, 20133, Milan, Italy. [4]IRCCS Istituto Ortopedico Galeazzi, Cell and Tissue Engineering Laboratory, via Galeazzi, 4, 20161, Milan, Italy. [5]Department of Orthaepedic Surgery and Rehabilitation, University of Nebraska Medical Center, Omaha, NE 68198, USA. [6]Iowa Institute for Oral Health Research, The University of Iowa, Iowa City, IA 52242, USA. [7]Department of Mechanical and Materials Engineering, University of Nebraska-Lincoln, Lincoln, NE 68588, USA.
*Corresponding author. Email: jingwei.xie@unmc.edu

RESULTS

Fabrication and characterization of RAS and VAS

RAS and VAS were fabricated by transformation of 2D electrospun nanofiber membranes through the solids of revolution-inspired gas-foaming expansion following our established protocols (*19*, *20*). Briefly, we cut the 2D mat consisting of uniaxially aligned nanofibers into a rectangular shape in liquid nitrogen. Then, we fixed one side of the rectangular mat by thermal treatment. When the fixed side was perpendicular to the direction of nanofiber alignment, we would obtain a cylindrical RAS after expansion. In contrast, when the fixed side was parallel to the direction of nanofiber alignment, we would obtain a cylindrical VAS after expansion. A scanning electron microscopy (SEM) image shows the top view of the RAS, displaying radially distributed channels formed by expanded, layered membranes consisting of aligned nanofibers along the radius direction, while the side view shows a porous structure (Fig. 1A). The inset images indicate the fiber alignment in the radial direction (Fig. 1A). In contrast, SEM images of the top view of the VAS reveal a highly porous structure formed by crimped, layered membranes consisting of aligned fibers along the axial direction, while the side view showing a channel structure (Fig. 1B). The inset images indicate the fiber alignment in the axial direction (Fig. 1B). The porosity and pore size of RAS and VAS can be tailorable by controlling the thickness of PCL nanofiber mat before expansion (fig. S1, A and B). The porosities of the RAS that were fabricated by expanding 0.5-, 1-, and 1.5-mm-thick PCL nanofiber mats were (80.81 ± 8.16%), (70.90 ± 5.6%), (49.80 ± 6.72%), respectively (fig. S1, C and D). The corresponding average pore sizes were (884.42 ± 439.92 μm), (283.12 ± 138.64 μm), and (106.86 ± 60.51 μm) accordingly. The porosities of the VAS that were fabricated by expanding 0.75-, 1-, and 1.5-mm-thick PCL nanofiber mats were (76.52 ± 4.93%), (68.60 ± 6.11%), (64.01 ± 5.27%), respectively. The average pore sizes were (1024.68 ± 357.01 μm), (417.39 ± 153.39 μm), and (246.84 ± 119.08 μm) accordingly.

It is observed that the pore size of the RAS and VAS gradually increased from the center to the edge. To quantify the pore size distribution in the RAS and VAS, four regions were defined from the center to the edge (Fig. 1, C and D). The average pore sizes in the regions 1 to 4 of the RAS were (57.45 ± 30.43 μm), (177.31 ± 36.96 μm), (331.21 ± 64.47 μm), and (494.33 ± 66.26 μm) (Fig. 1E). In comparison, the average pore sizes in the regions of 1 to 4 of the VAS were (129.09 ± 22.55 μm), (268.79 ± 53.50 μm), (503.43 ± 77.15 μm), and (872.06 ± 110.66 μm) (Fig. 1F). In addition, the channel lengths within the RAS and VAS were also quantified. The channel lengths in the RAS were mainly in the range of 2 to 2.5 mm, and the channels with a length over 2 mm accounted for 56.25% (Fig. 1, G and H). The channel lengths of the VAS were mainly in the range of 0.8 to 1 mm, and all the channels had a length over 0.6 mm (Fig. 1, I and J). For comparison, collagen sponges were examined by SEM, exhibiting a uniform porous structure in all dimensions and the average pore size was (143.42 ± 55.21 μm) (fig. S2). The mechanical properties of RAS and VAS in different directions were examined under

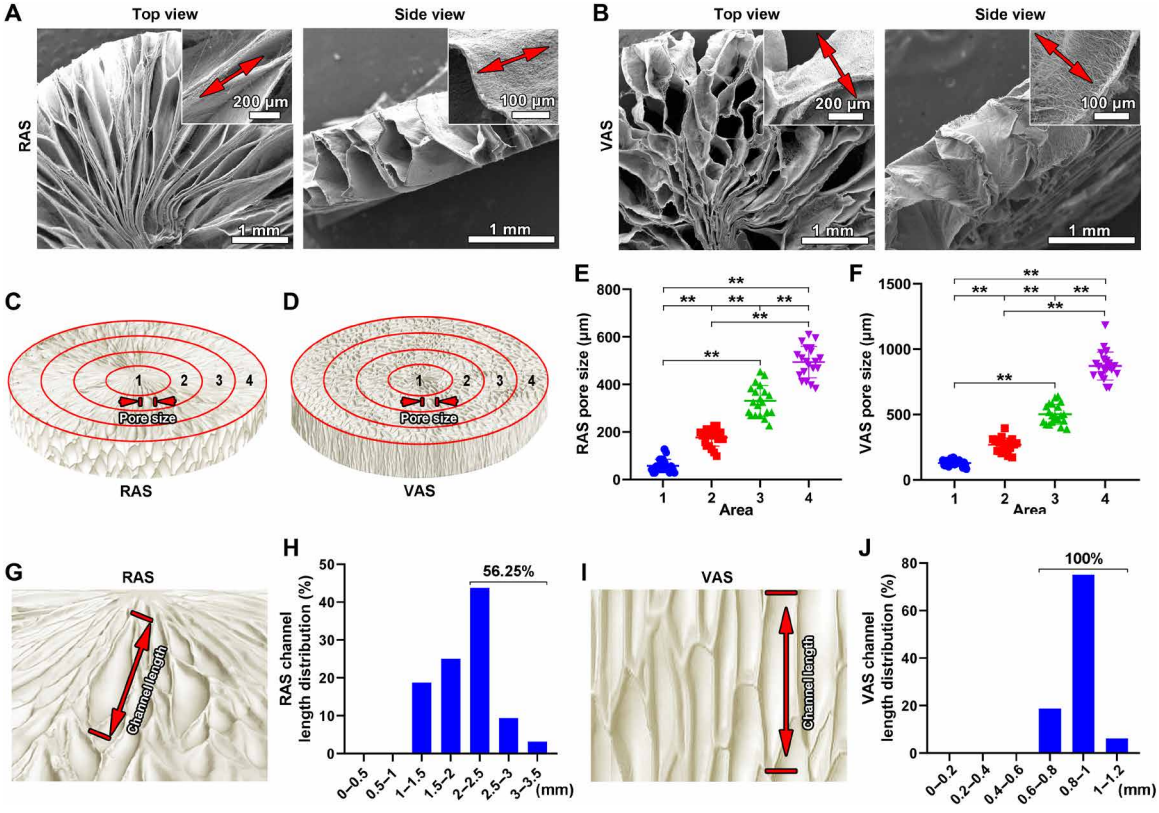

Fig. 1. Characterizations of RAS and VAS. (**A** and **B**) SEM images of the top view and side view of RAS and VAS. Insets: Highly magnified SEM images of (A) and (B) indicated the fiber alignment in RAS and VAS. (**C** and **D**) Schematic illustrating the four regions of RAS and VAS from the center to edge. (**E** and **F**) The corresponding average pore size of each region in RAS and VAS. (**G** and **H**) Schematic illustrating the channels along the radial direction of RAS and their corresponding length distribution. (**I** and **J**) Schematic illustrating the channels along the longitudinal direction of VAS and their corresponding length distribution. $^{**}P < 0.01$.

70% of compressive strain (fig. S3). The resultant compressive stresses of VAS in the side and frontal directions were similar (fig. S3). The compressive stress of RAS was much higher in the frontal direction than in the side direction when compressive strain was 70% (fig. S3).

RAS and VAS guide bone marrow stem cell migration and promote bone regeneration related gene expression

In the RAS, the open pores toward the surrounding healthy bone could guide and promote cell infiltration from the surrounding healthy bone to the defect site, while in the VAS, the open pores toward periosteum and dura could guide and promote cell infiltration from periosteum and dura to the defect site. Thus, we established two different in vitro migration models to examine the efficacy of RAS and VAS in guiding and promoting cell migration (fig. S4) (*20*). Bone marrow stem cells (BMSCs) were chosen for this study as they are the major and important cell source for bone regeneration (*21*). In the first model, the marginal BMSC migration was observed from the bottom to the top through RAS during 6 days of culturing, while the significant BMSC migration was detected from the bottom to the top through VAS (Fig. 2A). In particular, some BMSCs migrated to the top of VAS after 4 and 6 days of incubation (Fig. 2, A and B). In the second model, the sparsely distributed BMSCs were observed after 4 days of incubation, and more and more cells were detected after 8 and 12 days throughout the whole RAS, while BMSCs were mainly located at the edge of VAS during the incubating period (Fig. 2C and fig. S5). The migrated BMSCs covered the half surface of the RAS after 12 days of infiltration (Fig. 2D). The potential mechanism discovers that the BMSCs prefer to migrate from the bottom to the top within the VAS (Fig. 2, E and F) and from the edge to the center within the RAS (Fig. 2, G and H), which is mainly caused by the guiding role of aligned nanofibers on cell migration.

To investigate the expression of growth factors, extracellular matrix (ECM), proliferation, and apoptosis-related genes of BMSCs cultured on the RAS, we performed the heatmap analysis on the expression of BMP-2, basic fibroblast growth factor (bFGF), vascular endothelial growth factor (VEGF), platelet derived growth factor-BB (PDGF-BB), insulin-like growth factor 1 (IGF-1), transforming growth factor–β1 (TGF-β1), collagen 1, CXCR4, cyclin D1, CDK1, caspase-3, and BCL-2 genes of BMSCs on the RAS after culture for 5 and 9 days (Fig. 2I). The relative expression of BMP-2, bFGF, PDGF-BB, TGF-β1, type 1 collagen, CXCR4, and cyclin D1 of the BMSCs cultured on RAS was significantly increased compared to the BMSCs cultured in the petri dish after 5 days of incubation (Fig. 2J). After incubation for 9 days, the relative expression of BMP-2, bFGF, VEGF, PDGF-BB, IGF-1, TGF-β1, type 1 collagen, and cyclin D1 of the BMSCs cultured on RAS was significantly higher than those of the BMSCs cultured in petri dish (Fig. 2K). In addition, we also performed the heatmap analysis of BMSCs cultured on the VAS (fig. S6). By comparison, the VEGF relative expression of BMSCs was higher on the VAS than on the RAS. In addition, the cyclin D1 relative expression of BMSCs was lower on the VAS than on the RAS. The rest of tested markers for BMSCs showed similar expression levels on the VAS and RAS.

RAS and VAS accelerate cranial bone regeneration

To test the bone regeneration efficacy of RAS and VAS, we implanted these scaffolds into the critical-sized (8 mm in diameter) calvarial bone defects in rats (Fig. 3A) (*22*–*24*). The schematic diagrams indicate the open pores on the side of the RAS facing the bone marrow (Fig. 3B), and the open pores on the bottom and top of the VAS facing periosteum and dura matter after implantation, respectively (Fig. 3C). The schematic and surgical photographs reveal the treatment groups including control, RAS, VAS, and collagen sponges (fig. S7). After 4 and 8 weeks of implantation, the isolated tissues from bone defects and surrounding areas were imaged by micro–computed tomography (micro-CT). It is evident that more new bones were formed in both RAS and VAS groups compared to the control and collagen groups, particularly after 4 weeks of implantation (Fig. 3, D and E, and fig. S5). On the basis of the quantification from micro-CT images (*25*), the regenerated bone volume, surface coverage, and bone mineral density in the RAS group were markedly higher than those in the control, VAS, and collagen sponge groups (Fig. 3, F to H). The newly formed bone in the RAS and VAS groups showed a radially aligned structure and a honeycomb structure at both weeks 4 and 8, closely recapitulating the architectures of RAS and VAS (Fig. 3, D and E, and movies S1 and S2). In addition, the surface of the regenerated bone in the control and collagen sponge groups was smoother and flatter than the RAS and VAS groups (Fig. 3, D and E, and movies S3 and S4).

We further performed the trichrome staining of the isolated tissues from the defect sites and the surround areas. It is found that the defect sites in the control group were mainly filled with fibrotic tissues after 4 and 8 weeks of surgery (Fig. 3I and fig. S8). Only a small amount of new bone was formed at the edges of the defects (Fig. 3I and fig. S8). Similarly, the bone defects were mostly composed of fibrotic tissues after treatment of collagen sponges for 4 weeks (fig. S8). Although some newly formed bone tissues were detected in the collagen sponge group after 8 weeks of implantation, there was still a residual bone defect that did not completely close (Fig. 3I). In contrast, a large amount of newly formed bone was observed throughout the whole defect area in the RAS and VAS groups at as early as week 4, which were in line with the micro-CT results (Fig. 3, D and I). After 8 weeks of implantation, more regenerated bone tissues were seen over the entire defect regions in the RAS group that almost closed the defects (Fig. 3I). In both RAS and VAS groups, although no visible PCL nanofibers were seen within the newly formed bone tissues after 8 weeks, PCL nanofibers were not fully degraded because of their slow degradation rate. We speculate that the PCL nanofibers could be embedded within the newly formed bone tissues and integrate well with new tissues because of the high porosity and nanofibrous morphology of assemblies.

The second harmonic generation microscopy (SHGM) was used to characterize the organization of collagen fibers in the organic phase of the regenerated bone matrix after 8 weeks of operation (*26*, *27*). The SHGM images and the corresponding distributions of collagen fiber orientation were shown in Fig. 3J. It is observed that the orientation of collagen fibers in the organic phase of newly formed bone matrix was along the direction of nanofiber alignment in the RAS and VAS groups (Fig. 3J). On the contrary, collagen fibers were randomly distributed in the organic phase of newly formed bone matrix in the control and collagen sponge groups (Fig. 3J). The alignment score of collagen fibers of the RAS and VAS group was higher than the control and collagen groups (Fig. 3K). We also performed the type 2 collagen immunohistochemical staining (fig. S9). No visible type 2 collagen–positive areas were detected in the control and collagen groups because there was no significant new bone formation in these groups after 4 weeks of surgery (fig. S9A). The RAS and VAS groups had a significantly higher expression of type 2 collagen than

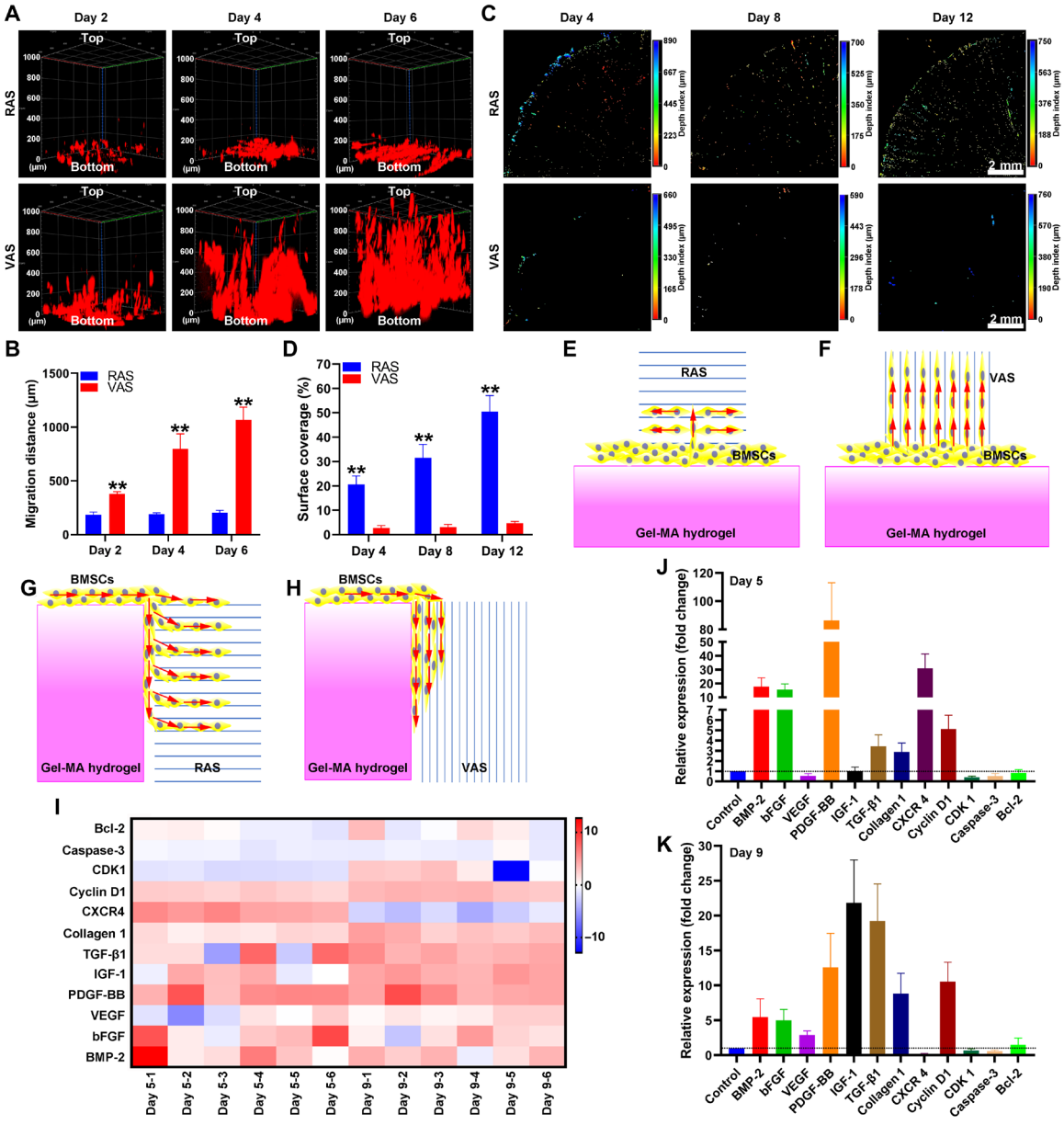

Fig. 2. 3D Nanotopographical cues promote the migration and bone regeneration–related gene expression of BMSCs. (**A**) Fluorescent images show the migration of BMSCs from the bottom to the top of RAS and VAS. (**B**) Quantification of the migrated distance of BMSCs from the bottom to the top of RAS and VAS. (**C**) Fluorescent images show the distribution of migrated BMSCs from the surrounding area to the center of the RAS and VAS. (**D**) The surface coverage of BMSCs migrated to RAS and VAS. (**E** and **F**) Schematic illustrating the possible migration route of BMSCs from the bottom to the top of RAS and VAS. (**G** and **H**) Schematic illustrating the possible migration route of BMSCs from the surrounding area to the center of RAS and VAS. (**I**) The heatmap shows the relative expression of BMP-2, bFGF, VEGF, PDGF-BB, insulin-like growth factor 1 (IGF-1), transforming growth factor–β1 (TGF-β1), Collagen 1, CXCR4, Cyclin D1, CDK1, Caspase-3, and BCL-2 of BMSCs cultured in RAS for 5 and 9 days. Blue color indicates down-regulation, and red color indicates up-regulation. (**J** and **K**) The relative expression of BMP-2, bFGF, VEGF, PDGF-BB, IGF-1, TGF-β1, Collagen 1, CXCR4, Cyclin D1, CDK1, Caspase-3, and BCL-2 of BMSCs cultured in RAS for 5 and 9 days. $^{**}P < 0.01$.

the control and collagen sponge groups at week 4 (fig. S9B). At week 8, RAS, VAS, and collagen sponge groups showed higher expression of type 2 collagen than the control group (fig. S9B). In addition, we did not find significant difference in the type 2 collagen expression among the RAS, VAS, and collagen sponge groups after 8 weeks of surgery (fig. S9B).

RAS and VAS guide the bone matrix formation

The bone ECM matrix consists of an organic phase (~30 to 40%) and an inorganic mineral phase (~60 to 70%) (*28*, *29*). To further understand the guidance of RAS and VAS, the decalcified, newly formed bone tissues (the organic phase of the regenerated bone matrix) was examined by SEM. It is confirmed that the top (close to periosteum)

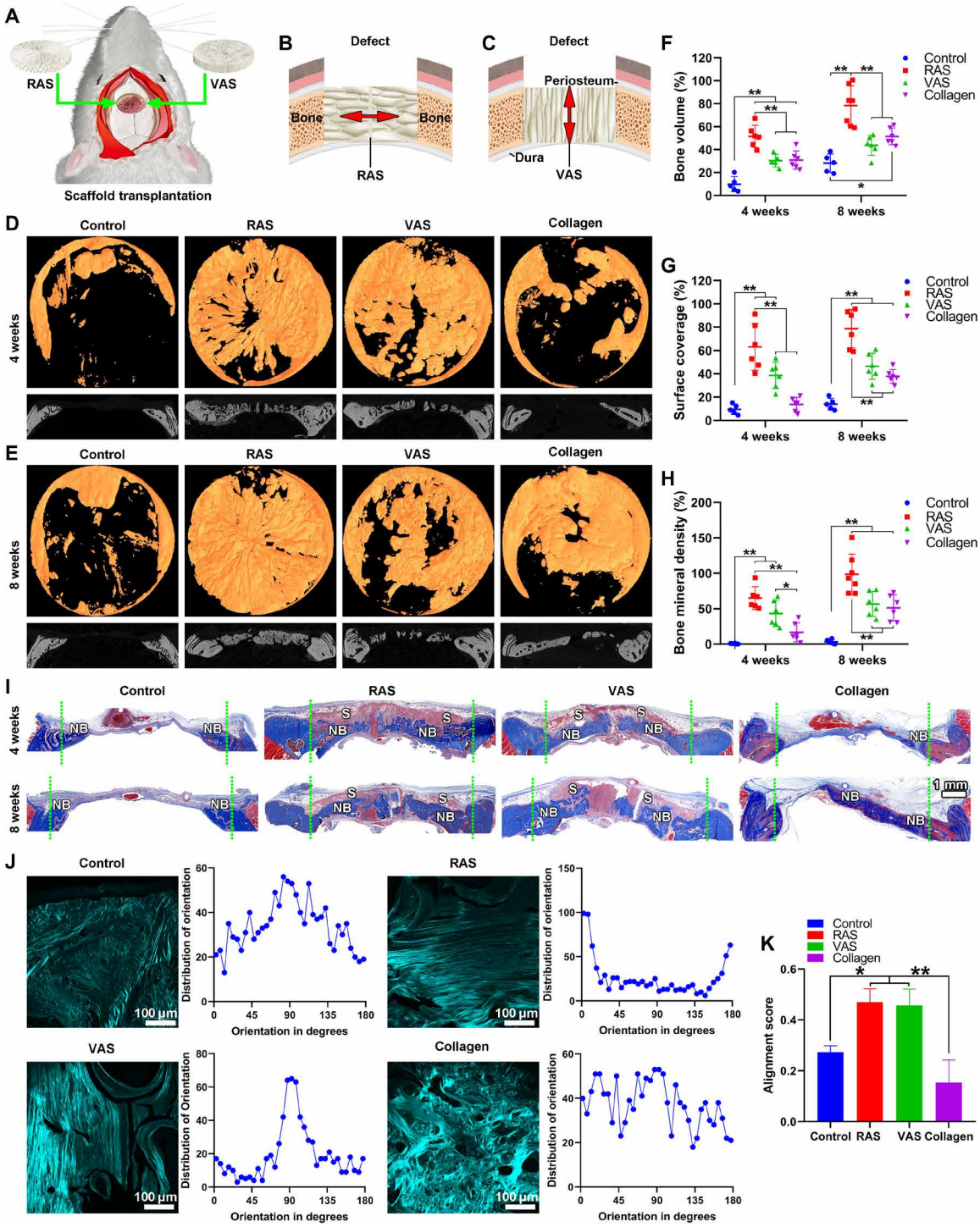

Fig. 3. RAS and VAS guides cranial bone regeneration. (**A** to **C**) Schematic illustrating the implantation of RAS and VAS to critical-sized cranial bone defects in rats and cross views of the interfaces between RAS, VAS, and surrounding tissues after implantation. (**D** and **E**) Micro-CT images of the control, RAS, VAS, and collagen sponge groups after 4 and 8 weeks of operation. (**F** to **H**) The regenerated bone volume (%), surface coverage (%), and bone mineral density (%) of the control, RAS, VAS, and collagen sponge groups after 4 and 8 weeks of operation. The bone volume and mineral density of the harvested cranial bone (8 mm in diameter) at the same surgical site from a 4-month-old rat are 32.18 mm^3 and 0.157 g/cm^3, respectively. The bone volume and mineral density of the harvested cranial bone (8 mm in diameter) at the same surgical site from a 5-month-old rat are 33.97 mm^3 and 0.171 g/cm^3, respectively. (**I**) The trichrome staining of isolated tissues from the control, RAS, VAS, and collagen sponge groups after 4 and 8 weeks of operation. Green dot lines indicate the edge of defects. S, scaffold; NB, new bone. (**J**) second harmonic generation microscopy (SHGM) images of collagen fibers in the organic phase of the regenerated bone and the corresponding distributions of orientations of collagen fibers after 8 weeks of operation. (**K**) The alignment score of the collagen fibers in the control, RAS, VAS, and collagen sponge groups after 8 weeks of operation. *$P < 0.05$, **$P < 0.01$. Control, no scaffold treatment.

and bottom (close to dura matter) parts of the native cranial bone are the compact bone exhibiting a layered, aligned structure. The middle part is the spongy bone exhibiting a random or partially aligned structure (Fig. 4A). Fibrotic tissues consisting of random fibers were mainly found in the defect sites in the control group at both weeks 4 and 8 (Fig. 4B). The organic phase of newly formed bone matrix at the edge of the defects showed a porous structure (fig. S10A). In contrast, the organic phase of the regenerated bone matrix showed a densely aligned structure after implantation of RAS for 4 and 8 weeks akin to that of the compact bone matrix (Fig. 4, A, B, and D). Differently, other than the fibrotic tissues (fig. S10B), the organic phase of the newly formed bone matrix showed an unordered, porous structure at the defect site after treatment of VAS for 4 weeks. The organic phase in the regenerated bone matrix may help illustrate how the new bone was formed within the VAS. The new bone could form underneath the VAS first due to BMSCs and bone progenitor cells migrated from the surrounding bone marrow and dura, and then the new bone could continuously grow from the bottom to the top of the VAS due to the migration of BMSCs or bone progenitor cells along the fiber alignment direction (fig. S10C). Most of the newly formed organic phase of the regenerated bone matrix within the VAS seemed immature after 4 weeks of implantation. A more mature organic phase in the regenerated bone matrix was noticed after implantation of VAS for 8 weeks (Fig. 4, B and E).

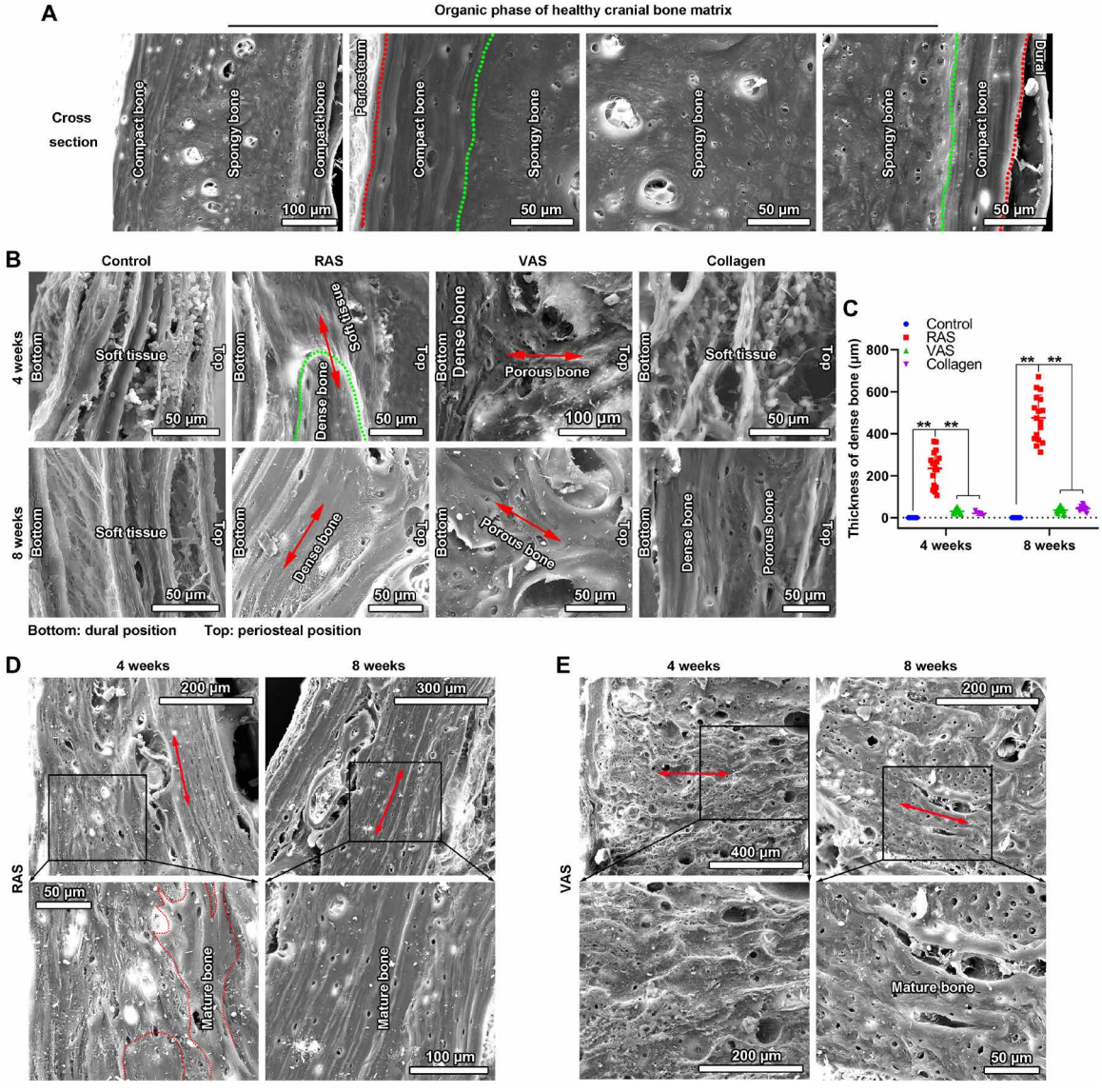

Fig. 4. RAS and VAS guide the formation of organic phase in regenerated cranial bone matrix. (**A**) SEM images show the organic phase of native cranial bone matrix after decalcification. The top and bottom parts are the compact bone with densely aligned structure. The middle part is the spongy bone with less dense and less ordered structure. (**B**) SEM images show the morphologies of the decalcified, regenerated bone tissues in the defect areas in the control, RAS, VAS, and collagen sponge groups after 4 and 8 weeks of operation. The red double arrows indicate the direction of nanofiber alignment. (**C**) Quantification of the thicknesses of regenerated bone matrix with densely aligned structure in the control, RAS, VAS, and collagen sponge groups after 4 and 8 weeks of operation. (**D** and **E**) The specified decalcified bone matrix of the RAS and VAS groups after 4 and 8 weeks of operation. The red double arrows indicate the direction of nanofibers. $^{**}P < 0.01$ Control, no scaffold treatment.

In addition, the bone defects showed a porous structure filling with a number of round shaped cells after implantation of collagen sponges for 4 weeks (Fig. 4B). The organic phase in the regenerated bone matrixes showed both the dense (bottom) and porous (top) regions after implantation of VAS for 8 weeks (Fig. 4B). The thickness of the organic phase in the regenerated bone matrix in the RAS group was significantly higher than the control, VAS, and collagen groups (Fig. 4C).

Besides the organic phase, we also analyzed the inorganic phase in the regenerated bone matrix based on micro-CT images. As shown in Fig. 5A, the inorganic phase of regenerated cranial bone was not very homogeneous. This could be due to the insufficient time of remodeling of regenerated bone as the duration for bone regeneration was only 8 weeks. The regenerated bone would undergo further remodeling, and the thickness of regenerated bone would eventually become similar to native bone after remodeling. In the microstructure, the mineral phase in native cranial bone showed a bridge structure containing some large pores. Large pores were also found in the newly formed minerals in the control and collagen sponge groups. In the contrast, smaller pores were observed in the newly created minerals in the RAS and VAS groups (Fig. 5, A and B). To further understand the mechanical function of regenerated bone, we evaluated the distribution of stress on the newly formed mineral phase after implantation for 8 weeks based on computational simulations using COMSOL Multiphysics. The colored whole image and three parallel section planes of the newly formed minerals in the control, VAS, and collagen sponge groups showed an uneven Mises stress distribution (Fig. 5C). In particular, in the VAS and collagen sponge groups, the high Mises stress existed around the large pore. An even Mises stress distribution was seen in the healthy cranial bone minerals and the newly formed mineral phase in the RAS group. In the present study, the stress distribution simulation based on the micro-CT data demonstrated that the internal structure of newly formed cranial bone was relatively uniform after implantation of RAS scaffolds, which is close to the normal cranial bone. The quantification of average Mises stress in the control, RAS, and VAS was higher than that in the healthy bone and RAS group. The mineral phase in the healthy cranial bone had a similar average Mises stress as the RAS group (Fig. 5D).

Biomaterials reveal the role of endogenous cells on cranial bone regeneration

To explore the contribution of endogenous cells to the cranial bone regeneration, we designed and tested three different configurations of biomaterials [RAS + nanofiber membranes for blocking cell penetration from the side and the bottom direction (SB), RAS + nanofiber membranes for blocking cell penetration from the side and the top direction (ST), and RAS + nanofiber membranes for blocking cell penetration from the top and the bottom direction (TB)] in the same critical-sized rat calvarial bone defect model (Fig. 6A). The nanofiber membranes for blocking cell penetration were made of pure PCL. The distributions of regenerated bone differed from one another among the SB, ST, and TB groups (Fig. 6, B to D, and fig. S11). Specifically, in the SB group, a large area of newly formed bone with limited thickness was detected underneath the nanofiber membrane placed on the bottom of RAS (Fig. 6, B to D, and movie S5). No evident new bone formation was seen within RAS (Fig. 6B). In the ST group, significant amount of new bone with a radially aligned structure was detected within RAS (Fig. 6, B to D). Meanwhile, a thin layer of bone was formed on the surface of the nanofiber membrane close to periosteum (Fig. 6B and movie S6). In the TB group, the regenerated bone tissues were distributed in three different regions including a thin layer of bone on the surface of nanofiber membrane adjacent to periosteum, a relative thick layer of bone underneath the nanofiber membrane facing dura matter, and a small amount of bone within RAS (Fig. 6B and movie S7). On the basis of the quantified micro-CT results, no significant difference in the regenerated bone volume was detected among the ST, SB, and TB groups after 4 and 8 weeks of operation (Fig. 6E). However, the surface coverage of the TB group was significantly higher than the ST and SB groups after 8 weeks of treatment (Fig. 6F). Besides, the mineral density of regenerated bone in the ST and TB groups were higher than the SB group (Fig. 6G). To confirm the micro-CT results, we further performed the trichrome staining of isolated tissues from bone defects and surrounding areas (Fig. 6H). It is verified that the newly formed bone was located underneath the nanofiber membrane in the SB group. There were two regions of new bone in the ST group. One was located on the surface of nanofiber membrane facing periosteum, and the other was inside RAS. Three distinct regions of new bone including the nanofiber membrane surface facing periosteum, within RAS, and the nanofiber membrane surface facing dura matter were observed in the TB group similar to the micro-CT results (Fig. 6, D and H).

DISCUSSION

Aligned nanotopographical cues have been widely demonstrated for positive regulation of cellular responses such as guiding and promoting cell migration and cell differentiation, holding great promise for tissue regeneration (*30*–*34*). However, current technologies are mainly limited to generation of the patterned grooves or aligned nanofiber membranes in a 2D form, which may not be able to match the geometric shape of tissue defects. To this end, we developed a solid of revolution inspired gas-foaming technique to convert traditional electrospun nanofiber mats into 3D objects with hierarchy structure and controlled alignment (e.g., RAS and VAS) (*19*, *20*). The RAS and VAS can promote not only BMSC migration along the direction of fiber alignment from the surrounding to the center and from the bottom to the top but also the expression of bone regeneration related genes in vitro. In vivo studies demonstrated RAS and VAS can guide endogenous bone regeneration rapidly as the regenerated bone within RAS and VAS showed a radially aligned pattern and a honeycomb pattern, closely recapitulating the architectures of RAS and VAS.

The cranial bone regeneration efficacy of RAS and VAS was much higher than the control and collagen sponge groups after 4 weeks of implantation, which was also far superior to the ones of reported biomaterials tested in the same animal model including the nanofiber aerogels, 3D-printed scaffolds, injectable thermo hydrogel, hybrid hydrogels, macroporous calcium phosphate, nanohydroxyapatite bone substitute, and deproteinized bovine bone (*23*, *24*, *35*–*40*). Furthermore, these biomaterials even incorporated with stem cells and therapeutic agents still had inferior performance relative to RAS and VAS (*36*, *38*, *40*). We speculate that the hierarchical structure and 3D aligned nanotopography in RAS and VAS could be critical for effective guidance of endogenous bone regeneration. We believe that the guidance and promotion of cell infiltration from specific directions are the keys for cranial bone

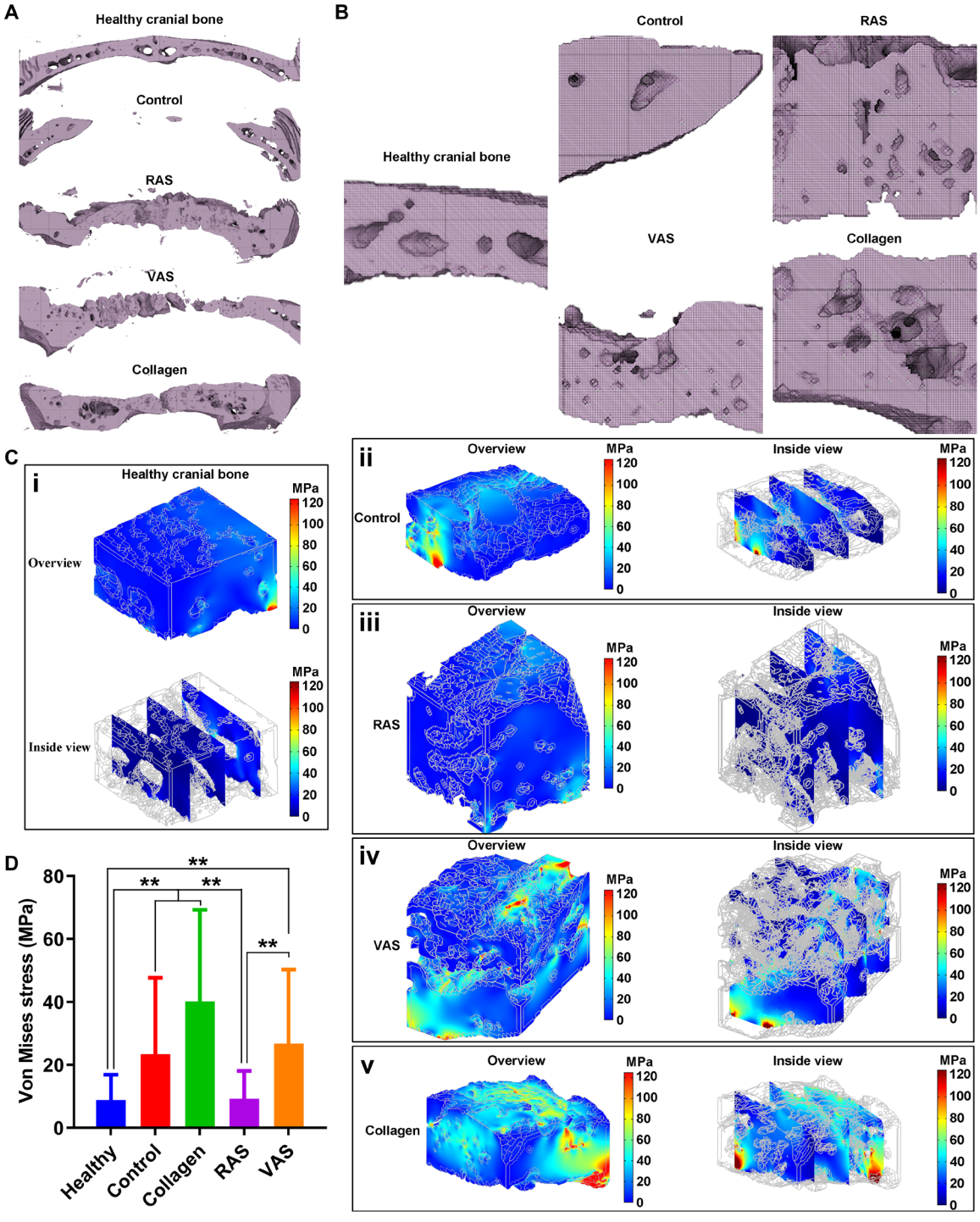

Fig. 5. RAS and VAS influence the configurations of the inorganic phase in regenerated cranial bone matrix. (**A**) Macrostructures of minerals within the native cranial bone and the regenerated bone tissues of the control, RAS, VAS, and collagen sponge groups. (**B**) High magnifications of (A). (**C**) Computational simulations of Von Mises stress distributions of control (ii), RAS (iii), VAS (iv), and collagen sponge (v) groups after 8 weeks of treatment. (**D**) Quantification of the average Von Mises stress in the native cranial bone, control, RAS, VAS, and collagen sponge groups after 8 weeks of treatment. $^{**}P < 0.01$. Healthy group is the cranial bone with the same age and without any surgery, which was used for comparison as a positive control. Control, no scaffold treatment.

regeneration. This is partially supported by the in vitro BMSC migration and heatmap analysis results. The directed and accelerated BMSC migration and enhanced expression of bone regeneration related genes in BMSCs may play important roles for repairing critical-sized cranial bone defects as the cranial vault bones are mainly formed by intramembranous ossification. The underlying molecular mechanism on the BMSC response regulated by 2D patterned surfaces was investigated previously, which could be

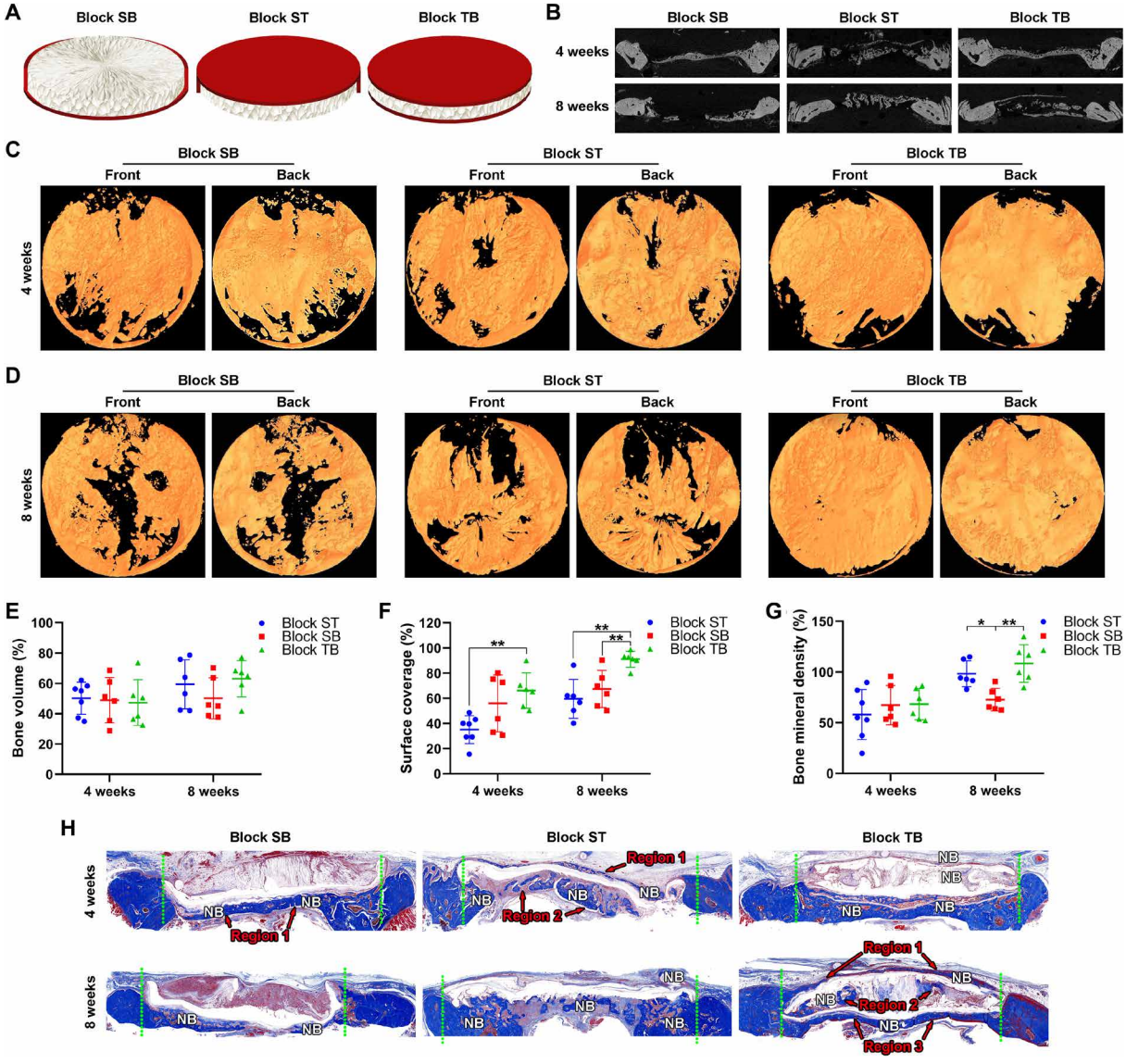

Fig. 6. Combining 2D nanofiber membranes with RAS reveals the roles of tissue sources on cranial bone regeneration. (**A**) Schematic illustrating the experimental designs including SB (RAS was attached by 2D nanofiber membranes on the lateral and bottom surfaces), ST (RAS was attached by 2D nanofiber membranes on the lateral and top surfaces), and TB (RAS was attached by 2D nanofiber membranes on the top and the bottom surfaces). (**B**) Micro-CT images show the cross sections of regenerated bone in the SB, ST, and TB groups after 4 and 8 weeks of operation. (**C** and **D**) Micro-CT images of the front and back views of regenerated bone in the SB, ST, and TB groups after 4 and 8 weeks of operation. (**E** to **G**) The regenerated bone volume (%), surface coverage (%), and mineral density (%) of the SB, ST, and TB groups after 4 and 8 weeks of operation. (**H**) Trichrome staining of regenerated bone tissues in SB, ST, and TB groups after 4 and 8 weeks of operation, indicating the distinct regions of newly formed bone in the SB, ST, and TB groups. Green dot lines indicate the edge of bone defects. *$P < 0.05$, **$P < 0.01$.

associated with the down-regulation of Zyxin protein expression in BMSCs (*41*). The decreased Zyxin expression may lead to smaller and more dynamic focal adhesion and reduced traction forces, resulting in faster and more directional migration of BMSCs. Such a mechanism could be used to explain the guidance and promotion of BMSCs cultured on RAS and VAS as well. In addition, the regenerated bone showed a radially aligned arrangement and a honeycomb pattern in RAS and VAS, closely mimicking the architectures of RAS and VAS, which could further confirm their guidance on endogenous bone regeneration. In addition, the positive immunohistochemical staining of type 2 collagen suggests that endochondral bone formation could play certain role in the new bone formation as well.

The regenerated ECM could provide indications of quality of newly formed bone tissues. The organic phase of the regenerated bone after demineralization showed a compact layered structure with certain alignment in the RAS group after 8 weeks of treatment, which seems similar to the structure of compact bone. This could be important as compact bone plays a dominant role in maintaining the mechanical property of the entire skull (*42*). The RAS group also

had much thicker densely packed organic matrix than other groups. In addition, on the basis of the SHG imaging results, the alignment score of collagen fibers in the RAS and VAS groups was higher than the control and collagen groups. However, the aligned collagen fibers only served as a temporary matrix that would be remodeled to native structure. The process of bone remodeling takes about 2 to 3 years. Furthermore, the inorganic phase of the regenerated ECM in the RAS group showed a uniform distribution of minerals with smaller pore size and lower Von Mises stress distribution when compared with other groups. On the basis of the structure of ECM and Von Mises stress simulation, regenerated bone in the RAS group may be able to endure higher mechanical stress, which could rapidly establish protection of the underlying brain. This type of biomaterials could also be useful for repairing bone defects of patients with osteoporosis as their bones are highly porous with low load bearing.

In addition, to reveal the contribution of different tissue sources to cranial bone regeneration in the RAS group, 2D nanofiber membranes served as a physical barrier were used to selectively inhibit cellular infiltration from different tissue sources due to their small pore size (*43*–*45*). Because of the high porosity, the membranes should have marginal influence on the diffusion of paracrine factors secreted by various tissue sources, nutrients, and wastes to the defect site (*45*). When the side and bottom of RAS were blocked by nanofiber membranes, although the top area of RAS was open for cell infiltration, new bone tissues preferred to form underneath the nanofiber membrane facing dura matter, resulting in a thin layer of regenerated bone. This result indicates the regenerated bone was likely attributed to the migration and differentiation of bone progenitor cells from surrounding bone marrow or dura matter. On the basis of the trichrome staining results, the nanofiber membranes effectively blocked cell infiltration into RAS from the side and bottom, and it seems that the regenerated bone was mainly contributed by the bone progenitor cells migrated from surrounding bone tissues to the sites below the nanofiber membrane facing dura matter. When the side and top of RAS were blocked by nanofiber membranes, the bottom of RAS was open for cell penetration. Unexpectedly, there were two regions of newly formed bone. The regenerated bone on the surface of nanofiber membrane facing periosteum could be due to the migration and differentiation of bone progenitor cells from surrounding bone tissues, while the newly formed bone within RAS may be attributed to the migration and differentiation of bone progenitor cells from dura matter or surrounding bone tissues. When the top and bottom of RAS were blocked by nanofiber membranes, the side of RAS was open for tissue ingrowth. The bone progenitor cells not only migrated along the top and bottom surface of the nanofiber membranes but also infiltrated into RAS through the side pores, resulting in formation of three regions of regenerated bone. These results suggest that the surrounding bone and dura matter play important roles in cranial bone regeneration, and the contribution of periosteum is marginal, which partially agrees with previous studies (*46*, *47*). In addition, the strategy presented in this study could inspire the design of next-generation biomaterials for effective guidance of endogenous tissue regeneration at a fast pace. Furthermore, our recent studies have examined the scale-up production of nanofiber assemblies, and the scaffolds with clinically relevant dimensions can be readily fabricated using a large electrospinning setup and a similar expansion procedure (*48*, *49*).

MATERIALS AND METHODS

Materials

Study design

This research is dedicated to the development of cell- and therapeutic agent–free biomaterials for effective repairing large calvarial bone defects that may be readily translated into clinical applications. 3D PCL nanofiber scaffolds coated with 0.5% gelatin were prepared reproducibly as bone grafts to guide the regeneration of 8-mm rat calvarial bone defects. These scaffolds were thoroughly characterized in terms of their morphology, structure, fiber alignment, porosity, and pore size. The in vitro migration and differentiation of BMSCs were further performed to illustrate the importance of aligned nanotopography rendered by 3D nanofiber scaffolds. The scaffolds were then implanted into 8-mm bone defects surgically created in rat skulls. The 8-mm rat cranial bone defect is a critical-sized defect that cannot heal on its own (*18*). This defect model was chosen to rigorously examine the in vivo efficacy of 3D nanofiber scaffolds with hierarchical structure and controlled alignment. All the rats were randomly assigned, and 12 rats were assigned to each group. The animal study was approved by Institutional Animal Care and Use Committee (IACUC) at the University of Nebraska Medical Center (UNMC). Bone regeneration was characterized by micro-CT after 4 and 8 weeks and histology. The collagen organization in the regenerated tissues after demineralization was characterized by SHGM. The distribution of stress on the regenerated mineral phase after 8 weeks was evaluated on the basis of the micro-CT images and computational simulations. The data obtained from all the rats were taken into consideration. In the presented figures, we used scatterplots to indicate the data obtained from the animal study.

Materials

PCL (molecular weight = 80 kDa), pluronic-F-127, gelatin, sodium borohydride, and Triton X-100 were purchased from Sigma-Aldrich (St. Louis, MO, USA). Dichloromethane (DCM) and *N*,*N*′-dimethylformamide (DMF) were purchased from BDH Chemicals (Dawsonville, GA, USA). Dulbecco's modified Eagle's medium, fetal bovine serum, and penicillin-streptomycin were obtained from Invitrogen (Carlsbad, CA, USA). Alexa Fluor 546 phalloidin was purchased from Abcam (Cambridge, MA, USA). Collagen bovine plugs were obtained from Integra LifeSciences Corporation (Plainsboro, NJ, USA). The RNeasy Mini Kit was ordered from QIAGEN (Hilden, Germany). All primers used for reverse transcription polymerase chain reaction (RT-PCR) test were purchased from Eurofins (Bothell, WA, USA). cDNA reverse transcription reagent kits were ordered from Quantabio (Beverly, MA, USA). SYBR Green detecting system was purchased from Bio-Rad (Hercules, CA, USA).

Fabrication of RAS, VAS, and collagen sponges

The RAS and VAS were prepared using a modified method from our previous studies (*15*, *16*). PCL/0.5% F127 nanofiber mats with a thickness of 1 mm were first produced by traditional electrospinning with a rotating mandrel as a collector. Two grams of PCL beads and 0.1 g of F127 were dissolved in 20 ml of DCM and DMF mixed solvent at a ratio of 4:1 (v/v), the final concentration of PCL is 10% and the final concentration of F127 is 0.5%. After PCL/F127 solution was completely dissolved, 50 ml of PCL/F127 solution was pumped at a flow rate of 0.7 ml/hour using a syringe pump while a potential of 18 kV was applied between the spinneret (22-gauge needle) and a grounded collector. Around 1-mm-thick uniaxially aligned PCL/F127 nanofiber mat was collected by a high-speed rotating drum. Subsequently, the mats were cut into rectangle shape in liquid nitrogen along the direction of nanofiber alignment or perpendicular

to the long axis of nanofibers [5 mm (width) × 15 mm (length)]. Then, the long side of these PCL/F-127 nanofiber mats was fixed by thermal treatment (85°C for 1 s). Subsequently, these mats were transferred into 1 M $NaBH_4$ solution and expanded for 30 min to form RAS and VAS. After expansion, the RAS and VAS were washed with distilled water under a vacuum (~200 Pa) for 10 s. This washing process was repeated three times. The distilled water was then removed, and the RAS and VAS were exposed to a vacuum until it froze and then freeze-dried. The RAS and VAS were further coated with a 0.5% gelatin solution for 10 min to enhance their mechanical property. These 3D scaffolds were exposed to a vacuum until they froze and then freeze-dried after the residual gelatin solution was removed. Last, the gelatin-coated RAS and VAS with a height of 15 mm were cut into RAS and VAS with a height of 1 mm. The RAS and VAS with a thickness of 1 mm were further punched by an 8-mm punch. Similarly, the collagen sponges were made by cutting and punching the commercial absorbable collagen bovine plugs into disks (diameter: 8 mm; thickness: 1 mm).

Fabrication of RAS and VAS with different porosities and pore sizes

Briefly, the 0.5-, 1-, and 1.5-mm-thick PCL/0.5% F-127 nanofiber mats were cut into pieces [5 mm (width) × 15 mm (length)] with rectangle shape along the direction perpendicular to the long axis of nanofibers. These mats were also cut into pieces [5 mm (width) × 15 mm (length)] with rectangle shape along the direction of long axis of nanofibers. Then, the expansion, gelatin coating, and punching processes were performed as abovementioned. Last, the RAS and VAS with different porosities and pore sizes were obtained.

Fabrication of ST, SB, and TB

The RAS with 1 mm in thickness and 8 mm in diameter were prepared as described above. PCL nanofiber mats with 200 μm thick were prepared following our previous studies. ST was fabricated by covering the side and top surface of RAS with nanofiber mats. SB was fabricated by covering the side and bottom surface of RAS with nanofiber mats. TB was fabricated by covering the top and bottom surfaces of RAS with nanofiber mats. All the covered nanofiber mats were fixed to RAS with DCM solvent. Last, ST, SB, and TB were placed in the fume hood for 3 days to remove the residual DCM solvent.

Characterization of biomaterials

The RAS, VAS, collagen sponges, and tissue samples isolated from the control, RAS, VAS, and collagen sponge groups and sectioned by cryo-cutting were coated with Pt for 5 min using a Pt sputter coater and imaged by a SEM under 25 kV (FEI, Quanta 200, Billerica, MA, USA). The porosities and pore sizes of RAS and VAS expanded from 0.5-, 1-, and 1.5-mm nanofiber mats (fig. S1) were measured by mercury porosimetry (Micromeritics, AutoPore IV 9500, IL, USA). The average pore size of each region in RAS and VAS (Fig. 1, C to F) was measured on the basis of the SEM images. The channel length of the RAS and VAS (Fig. 1, G to J) were also measured on the basis of the SEM images.

Mechanical tests

The mechanical properties of RAS and VAS were examined in the frontal and side directions, which are defined in fig. S3C. The compressive stress was recorded with an Instron 5640 universal test machine with a 10-N load. For the tests in the frontal direction, the compressive strain of RAS (4 mm in height, 8 mm in diameter) and VAS (4 mm in height, 8 mm in diameter) was set as 70% (maximum compressive strain of RAS and VAS). For the tests in the side direction, the compressive strain of RAS (4 mm in length, 4 mm in height, 4 mm in width) and VAS (4 mm in length, 4 mm in height, 4 mm in width) was the same as the one used in the frontal direction.

BMSC migration on RAS and VAS

The gelatin methacryloyl (Gel-MA) was sterilized with ethylene oxide for 12 hours. Then, 8% (w/v) of Gel-MA solution with 0.05% (w/v) 2959 photoinitiator was prepared in 0.01 M phosphate-buffered saline (PBS) buffer (pH 7.4), and 3 ml of the mixed solution was added into each well of the six-well plate and cross-linked with ultraviolet light for 1 min. The Gel-MA hydrogels were washed three times with 0.01 M PBS before use. BMSCs were isolated from Sprague-Dawley rats (male, 6 months old) following standard procedures. The fourth-generation of BMSCs was used for the migration study. One milliliter of BMSCs solution (1×10^7 cells/ml) was seeded on the surface of 8% Gel-MA hydrogel and cultured until the cell confluence reached 90%. Two different in vitro migration models were established. In the first model, the RAS or VAS were placed on the surface of BMSCs seeded Gel-MA hydrogel and continuously cultured for 2, 4, and 6 days. In the second model, an 8-mm hole was created by a punch, and then RAS or VAS were inserted into the hole. The surface of scaffolds and the surface of hydrogel were kept at the same level and then continuously cultured for 4, 8, and 12 days.

Immunofluorescent staining and confocal imaging

The BMSCs seeded on the surface of Gel-MA hydrogel without or with an 8-mm hole were fixed with 4% paraformaldehyde and permeabilized with a 0.1% Triton X-100 solution in PBS. Subsequently, the BMSCs were stained with Alexa Fluor 546 phalloidin (dilution 1:200) for 20 min. Then, the BMSCs seeded on the surface of Gel-MA hydrogel without or with an 8-mm hole were imaged by confocal laser scanning microscopy (CLSM) (Zeiss 880, Oberkochen, Germany). The z-stack range was set from 0 to 250 μm, the interval was set at 10 μm, and the tile scans were set as 2 × 2 for hydrogel without a hole, and 7 × 7 for hydrogel with an 8-mm hole. At each indicated time point, the BMSCs infiltrated RAS and VAS were collected and fixed with 4% paraformaldehyde and permeabilized with a 0.1% Triton X-100 solution in PBS. Then, the scaffolds were stained with Alexa Fluor 546 phalloidin (dilution 1:400) for 20 min. Last, the RAS and VAS were imaged by CLSM. In the first migration model, the z-stack range was set from 0 to 1000 μm, and the interval was set at 10 μm. In the second migration model, the z-stack range was set from 0 to 900 μm, the interval was set at 10 μm, and the tile scan was set as 7 × 7.

Reverse transcription polymerase chain reaction

BMSCs were seeded on the RAS for 5 and 9 days. The BMSCs seeded on wells of a six-well culture plate for 5 and 9 days were used as control. At each indicated time point, the BMSCs seeded RAS was placed into RNA-free bead tubes and blended with a bullet blender. The total RNA was extracted using the RNeasy Mini Kit according to the manufacturer's instructions. One microgram of RNA was used to synthesize cDNA using a reverse transcription reagent kit. Then, the relative expression of BMP-2, bFGF, VEGF, PDGF-BB, IGF-1, TGF-β1, type 1 Collagen, CXCR4, Cyclin D1, CDK1, Caspase-3, and BCL-2 was measured by the RT-PCR based on SYBR Green detecting system, which was performed using an Applied Biosystems 7500 Fast Real-time PCR system (Applied Biosystems, USA) with the following temperature profile: at 95°C for 3 min, then 40 cycles at 95°C for 3 s, and at 60°C for 30 s. All primer sequences were as follows:

BMP-2 forward primer: CACGAGAATGGACGTGCCC, reverse primer: GGGAAGCAGCAACACTAGAAG;

bFGF forward primer: TCCATCAAGGGAGTGTGTGC, reverse primer: TCCGTGACCGGTAAGTGTTG;

VEGF forward primer: GGGTCAAAAACGAAAGCGCA, reverse primer: TACACGTCTGCGGATCTTGG;

PDGF-BB forward primer: CAAGACGCGTACAGAGGTGT, reverse primer: GCACTGCACATTGCGGTTAT;

IGF-1 forward primer: AGATGTACTGTGCTCCG, reverse primer: GCAAAGGATCTTGCGGTGAC;

TGF-β1 forward primer: AGGGCTACCATGCCAACTTC, reverse primer: CCACGTAGTAGACGATGGGC;

type 1 collagen forward primer: GGAGAGAGCATGACCGATGG, reverse primer: GGGACTTCTTGAGGTTGCCA;

CXCR4 forward primer: GCCATGGCTGACTGGTACTT, reverse primer: CACCCACATAGACGGCCTTT;

Cyclin D1 forward primer: AGGTCCCCTTGGGATGTGTT, reverse primer: CTCCCTATACTCAGGGTGATGC;

CDK1 forward primer: GGAACAGAGAGGGTCCGTTG, reverse primer: AGAGATTTCCCGGATTGCCG;

Caspase-3 forward primer: GGAGCTTGGAACGCGAAGAA, reverse primer: ACACAAGCCCATTTCAGGGT;

BCL-2 forward primer: CTGGTGGACAACATCGCTCT, reverse primer: GCATGCTGGGGCCATATAGT.

Critical-sized rat calvarial bone defect model

Ninety-one Sprague-Dawley rats (male, 3 months of age, 380 to 420 g) were used for the in vivo study. The rat was anesthetized using 4% isoflurane in oxygen for approximately 2 min. Then, rat scalp was shaved and sterilized with povidone-iodine for 3 min and cleaned three times with ethanol swabs. The skin, subcutaneous tissue, and periosteum were sequentially incised to expose the calvaria. A critical-sized cranial bone defect (8 mm in diameter) was created by using a trephine bur mounting on a dentist drill. The saline solution was continuously added to reduce the temperature during drilling. In addition, the dura mater was kept intact when the defect was successfully created. Different treatments were applied to the defects, and then the periosteum was sutured with an absorbable suture and the skin was sutured with a nonabsorbable suture. During the surgery, the rat was placed on a heating pad to maintain its body temperature. The defects without any treatment were set as the control group (no scaffold) (n = 13). The defects treated with the RAS were set as the RAS group (n = 13). The defects treated with the VAS were set as the VAS group (n = 13). The defects treated with the collagen scaffold were set as the collagen group (n = 13). The defects treated with ST were set as the ST group (n = 13). The defects treated with SB were set as the SB group (n = 13). The defects treated with TB were set as the TB group (n = 13). The rats were individually housed after surgery. Euthanasia by CO_2 asphyxiation was performed on the rats after 4 and 8 weeks of surgery. The rat craniums together with the dura were isolated and fixed in 10% formalin for 3 days and then transferred to 70% ethanol for micro-CT scanning.

Micro-CT scanning and data analysis

All cranial bone samples were scanned with a high-resolution micro-CT scanner (Skyscan 1172, Bruker). The scanning parameters including voltage (44 kV), current (226 μA), and image pixel size (8.62 μm) were used. The analysis of bone volume and bone mineral density was performed by CTAn software (Bruker). The surface coverage of regenerated bone was calculated by ImageJ. The 3D reconstruction of the whole cranial bone was performed by CTvol (Bruker). The bone volume and bone mineral density of healthy cranial bone at the age of 4 and 5 months were used as a reference for comparison among the control, RAS, VAS, and collagen sponge groups after 4 and 8 weeks of implantation.

Computational simulations

We performed computational simulations to evaluate the distribution of Von Mises stress on tested configurations using COMSOL Multiphysics (COMSOL Inc., Burlington, MA, USA). To optimize the STL files exported from the CT scanner, we used the free software Meshmixer (Autodesk Inc., Mill Valley, CA, USA) to smooth the surfaces with the Mesh Smoothing tool, repair the STL errors with the Auto-Repair function, and lastly adequately cut the models. We exported the refined models as new STL files and imported them to COMSOL. To keep the number of elements within a manageable range and the low computational cost, we extracted small portions (1 mm × 1 mm × 1 mm) from the whole reconstructed mineral structures. We applied the Solid Mechanics interface for the structural analysis of 3D models, considering bone as an isotropic linear elastic material. For configurations in healthy, control, RAS, VAS, and collagen sponge groups, we set the Young's modulus (E) equal to 0.022 GPa, the average Young's modulus of rat cranial bone. We set a Poisson's coefficient (ν) equal to 0.3 for all the configurations and a value of density dependent on the measured density of the tested structures (range, 5.62 to 171.88 kg/m^3). We set a boundary load to apply a total force of 5 N on the top surface of the models and a fixed constraint on the bottom surface, calculating the solutions of a stationary study. We created a tetrahedral mesh with up to 160,000 elements, and we evaluated the distribution of Von Mises stress on the surface of the models and on three section planes, cut starting from the middle section plane.

Masson trichrome staining

After the micro-CT scanning, the decalcification of all isolated samples was performed with 10% EDTA solution (pH 7.4) for 4 weeks, and the EDTA solution was changed every week. All decalcified cranial bones were cut along the middle of the defects. All samples were dehydrated in a graded ethanol series (70 to 100%), embedded in paraffin, and then 5-μm-thick paraffin slides were prepared for histological. The Masson trichrome staining was performed using standard protocols in the Tissue Science Facility at UNMC.

Orientation of collagen fibers

Collagen SHG imaging was conducted at the Multiphoton Intravital and Tissue Imaging core using an upright Olympus FVMPE-RS microscope equipped with a Spectra-Physics InSight X3 laser and 25× (1.05 numerical aperture) objective. SHG images were collected using 860-nm excitation with SHG-specific emission collected using a 432-nm (45 nm bandpass) emission filter. Collagen organization and alignment were quantified in individual SHG images (509 μm × 509 μm × 5 μm, 0.497 μm/pixel) using CT-FIRE and CurveAlign for Fibrillar Collagen Quantification software (see References below). Collagen alignment was calculated as the average of measurements obtained from 200-μm regions of interest within each image.

Immunohistochemical staining

The immunohistochemical staining was performed following procedures previously described (*50*). The slides were deparaffinized and rehydrated followed by antigen retrieval in heated citrate buffer for 5 min (citrate buffer solution, pH 6.0 at 100°C). Nonspecific antibody binding was prevented with a 5% bovine serum albumin solution. The sections were incubated with type 2 collagen primary antibodies overnight at 4°C. Then, the corresponding secondary antibodies were added and incubated for 1 hour at room temperature,

followed by incubating for 30 min with prepared VECTASTAIN ABC-alkaline phosphate (AP) reagent and then incubating with AP substrate solution for 20 min. Ten randomly selected fields were examined for each group at each time point and used to assess the average positive cells per unit area.

Statistical analysis

All data were presented as means ± SD. The statistical analysis was performed using GraphPad Prism 8.0 software. Differences among groups were evaluated using one-way analysis of variance (ANOVA) followed by Tukey's multiple comparisons test. The values of $P < 0.05$ were considered statistically significant. The values of $P < 0.01$ were considered statistically very significant.

SUPPLEMENTARY MATERIALS

Supplementary material for this article is available at http://advances.sciencemag.org/cgi/content/full/7/31/eabg3089/DC1

View/request a protocol for this paper from *Bio-protocol*.

REFERENCES AND NOTES

1. S. Lam, J. Kuether, A. Fong, R. Reid, Cranioplasty for large-sized calvarial defects in the pediatric population: A review. *Craniomaxillofac. Trauma Reconstr.* **8**, 159–170 (2015).
2. C. Szpalski, J. Barr, M. Wetterau, P. B. Saadeh, S. M. Warren, Cranial bone defects: Current and future strategies. *Neurosurg. Focus* **29**, E8 (2010).
3. M. E. Elsalanty, D. G. Genecov, Bone grafts in craniofacial surgery. *Craniomaxillofac. Trauma Reconstr.* **2**, 125–134 (2009).
4. K. L. Christman, Biomaterials for tissue repair. *Science* **363**, 340–341 (2019).
5. A. W. James, G. LaChaud, J. Shen, G. Asatrian, V. Nguyen, X. Zhang, K. Ting, C. Soo, A review of the clinical side effects of bone morphogenetic protein-2. *Tissue Eng. Part B Rev.* **22**, 284–297 (2016).
6. C. T. Laurencin, K. M. Ashe, N. Henry, H. M. Kan, K. W. H. Lo, Delivery of small molecules for bone regenerative engineering: Preclinical studies and potential clinical applications. *Drug Discov. Today* **19**, 794–800 (2014).
7. J. C. Lee, E. J. Volpicelli, Bioinspired collagen scaffolds in cranial bone regeneration: From bedside to bench. *Adv. Healthc. Mater.* **6**, 1700232 (2017).
8. S. Wang, Y. Yang, Z. Zhao, X. Wang, A. G. Milkos, Z. Qiu, T. Song, X. Sun, L. Zhao, C. Zhang, F. Cui, Mineralized collagen-based composite bone materials for cranial bone regeneration in developing sheep. *ACS Biomater. Sci. Eng.* **3**, 1092–1099 (2017).
9. D. Hoffman-Kim, J. A. Mitchel, R. V. Bellamkonda, Topography, cell response, and nerve regeneration. *Ann. Rev. Biomed. Eng.* **12**, 203–231 (2010).
10. A. Curis, C. Wilkinson, Topographical control of cells. *Biomaterials* **18**, 1573–1583 (1997).
11. K. Chung, J. A. DeQuach, K. L. Christman, Nanopatterned interfaces for controlling cell behavior. *Nano Life* **01**, 63–77 (2010).
12. M. Ventre, C. T. Natale, C. Rianna, P. A. Netti, Topographic cell instructive patterns to control cell adhesion, polarization and migration. *J. R. Soc. Interface* **11**, 20140687 (2014).
13. M. J. Dalby, N. Gadegaard, R. Tare, A. Andar, M. O. Riehle, P. Herzyk, C. D. W. Wilkinson, R. O. C. Oreffo, The control of human mesenchymal cell differentiation using nanoscale symmetry and disorder. *Nat. Mater.* **6**, 997–1003 (2007).
14. K. Duval, H. Grover, L. H. Han, Y. Mou, A. F. Pegoraro, J. Fredberg, Z. Chen, Modeling physiological events in 2D vs 3D cell culture. *Physiology* **32**, 266–277 (2017).
15. E. M. Bueno, J. Glowacki, Cell-free and cell-based approaches for bone regeneration. *Nat. Rev. Rheumatol.* **5**, 685–697 (2009).
16. M. A. Woodruff, D. W. Hutmacher, The return of a forgotten polymer-polycaprolactone in the 21st century. *Prog. Polym. Sci.* **35**, 1217–1256 (2010).
17. E. F. Eriksen, Cellular mechanisms of bone remodeling. *Rev. Endocr. Metab. Disord.* **11**, 219–227 (2010).
18. M. Santoro, A. M. Tatara, A. G. Mikos, Gelatin carriers for drug and cell delivery in tissue engineering. *J. Control. Release* **190**, 210–218 (2014).
19. S. Chen, H. Wang, A. McCarthy, Z. Yan, H. J. Kim, M. A. Carlson, Y. Xia, J. Xie, Three-dimensional objects consisting of hierarchically assembled nanofibers with controlled alignments for regenerative medicine. *Nano Lett.* **19**, 2059–2065 (2019).
20. S. Chen, A. McCarthy, J. V. John, Y. Su, J. Xie, Converting 2D nanofiber membranes to 3D hierarchical assemblies with structural and compositional gradients regulates cell behavior. *Adv. Mater.* **32**, 2003754 (2020).
21. C. Zheng, J. Chen, S. Liu, Y. Jin, Stem cell-based bone and dental regeneration: A view of microenvironmental modulation. *Int. J. Oral Sci.* **11**, 23 (2019).
22. P. P. Spicer, J. D. Kretlow, S. Young, J. A. Jansen, F. K. Kasper, A. G. Mikos, Evaluation of bone regeneration using the rat critical size calvarial defect. *Nat. Protoc.* **7**, 1918–1929 (2012).
23. L. Weng, S. K. Boda, H. Wang, M. J. Teusink, F. D. Shuler, J. Xie, Novel 3D hybrid nanofiber aerogels coupled with BMP-2 peptides for cranial bone regeneration. *Adv. Healthc. Mater.* **7**, 1870042 (2018).
24. R. Li, H. Wang, J. V. John, H. Song, M. J. Teusink, J. Xie, 3D hybrid nanofiber aerogels combining with nanoparticles made of a biocleavable and targeting polycation and MiR-26a for bone repair. *Adv. Funct. Mater.* **30**, 2005531 (2020).
25. M. L. Bouxsein, S. K. Body, B. A. Christiansen, R. E. Guldberg, K. L. Jepsen, R. Muller, Guidelines for assessment of bone microstructure in rodents using micro-computed tomography. *J. Bone Miner. Res.* **25**, 1468–1486 (2010).
26. A. Petersen, A. Princ, G. Korus, A. Ellinghaus, H. Leemhuis, A. Herrera, A. Klaumünzer, S. Schreivogel, A. Woloszyk, K. Schmidt-Bleek, S. Geissler, I. Heschel, G. N. Duda, A biomaterial with a channel-like pore architecture induces endochondral healing of bone defects. *Nat. Commun.* **9**, 4430 (2018).
27. J. S. Bredfeldt, Y. Liu, C. A. Pehlke, M. W. Conklin, J. M. Szulczewski, D. R. Inman, P. J. Keely, R. D. Nowak, T. R. Mackie, K. W. Eliceiri, Computational segmentation of collagen fibers from second-harmonic generation images of breast cancer. *J. Biomed. Opt.* **19**, 016007 (2014).
28. B. W. M. De Wildt, S. Ansari, N. A. J. M. Sommerdijk, K. Ito, A. Akiva, S. Hofmann, From bone regeneration to three-dimensional in vitro models: Tissue engineering of organized bone extracellular matrix. *Curr. Opin. Biomed. Eng.* **10**, 107–115 (2019).
29. K. Farbod, M. R. Nejadnik, J. A. Jansen, S. C. G. Leeuwenburgh, Interactions between inorganic and organic phases in bone tissue as a source of inspiration for design of novel nanocomposites. *Tissue Eng. Part B Rev.* **20**, 173–188 (2014).
30. C. J. Bettinger, R. Langer, J. T. Borenstein, Engineering substrate topography at the micro- and nanoscale to control cell function. *Angew. Chem. Int. Ed.* **48**, 5406–5415 (2009).
31. D. H. Kim, P. P. Provenzano, C. L. Smith, A. Levchenko, Matrix nanotopography as a regulator of cell function. *J. Cell Biol.* **197**, 351–360 (2012).
32. Y. Yang, K. Wang, X. Gu, K. W. Leong, Biophysical regulation of cell behavior-cross talk between substrate stiffness and nanotopography. *Engineering* **3**, 36–54 (2017).
33. J. Xue, T. Wu, Y. Xia, Perspective: Aligned arrays of electrospun nanofibers for directing cell migration. *APL Mater.* **6**, 120902 (2018).
34. A. Jain, M. Betancur, G. D. Patel, C. M. Valmikinathan, V. J. Mukhatyar, A. Vakharia, S. B. Pai, B. Brahma, T. J. MacDonald, R. V. Bellamkonda, Guiding intracortical brain tumour cells to an extracortical cytotoxic hydrogel using aligned polymeric nanofibres. *Nat. Mater.* **13**, 308–316 (2014).
35. Y. H. Huang, A. E. Jakus, S. W. Jordan, Z. Dumanian, K. Parker, L. Zhao, P. K. Patel, R. N. Shah, Three-dimensionally printed hyperelastic bone scaffolds accelerate bone regeneration in critical-size calvarial bone defects. *Plast. Reconstr. Surg.* **143**, 1397–1407 (2019).
36. S. J. Stephan, S. S. Tholpady, B. Gross, C. E. Petrie-Aronin, E. A. Botchway, L. S. Nair, R. C. Ogle, S. S. Park, Injectable tissue-engineered bone repair of a rat calvarial defect. *Laryngoscope* **120**, 895–901 (2010).
37. S. J. Lee, H. Nah, D. N. Heo, K.-H. Kim, J. M. Seok, M. Heo, H.-J. Moon, D. Lee, J. S. Lee, S. Y. An, Y.-S. Hwang, W.-Y. Ko, S. J. Kim, S. Sohn, S. A. Park, S.-Y. Park, I. K. Kwon, Induction of osteogenic differentiation in a rat calvarial bone defect model using an in situ forming graphene oxide incorporated glycol chitosan/oxidized hyaluronic acid injectable hydrogel. *Carbon* **168**, 264–277 (2020).
38. A. K. Teotia, D. B. Raina, C. Singh, N. Sinha, H. Isaksson, M. Tagil, L. Lidgren, A. Kumar, Nano-hydroxyapatite bone substitute functionalized with bone active molecules for enhanced cranial bone regeneration. *ACS Appl. Mater. Interfaces* **9**, 6816–6828 (2017).
39. N. Mokbel, C. B. Sehal, G. Matni, N. Naaman, Healing patterns of critical size bony defects in rat following bone graft. *Oral Maxillofac. Surg.* **12**, 73–78 (2008).
40. H. H. K. Xu, P. Wang, L. Wang, C. Bao, Q. Chen, M. D. Weir, L. C. Chow, L. Zhao, X. Zhou, M. A. Reynolds, Calcium phosphate cements for bone engineering and their biological properties. *Bone Res.* **5**, 17056 (2017).
41. K. Kulangara, Y. Yang, J. Yang, K. W. Leong, Nanotopography as modulator of human mesenchymal stem cell function. *Biomaterials* **33**, 4998–5003 (2012).
42. J. A. Motherway, P. Verschueren, G. Van der Perre, J. Vander Sloten, M. D. Gilchrist, The mechanical properties of cranial bone: The effect of loading rate and cranial sampling position. *J. Biomech.* **42**, 2129–2135 (2009).
43. M. Alimohammdi, Y. Aghli, O. Fakhraei, A. Moradi, M. Passandideh-Fard, M. H. Ebrahimzadeh, A. Khademhosseini, A. K. Tamayol, S. A. M. Shaegh, Electrospun nanofibrous membranes for preventing tendon adhesion. *ACS Biomater. Sci. Eng.* **6**, 4356–4376 (2020).
44. C. H. Chen, S. H. Chen, K. T. Shalumon, J. P. Chen, Dual functional core-sheath electrospun hyaluronic acid/polycaprolactone nanofibrous membranes embedded with silver nanoparticles for prevention of peritendinous adhesion. *Acta Biomater.* **26**, 225–235 (2015).

45. S.-H. Chen, C.-H. Chen, Y. T. Fong, J.-P. Chen, Prevention of peritendinous adhesions with electrospun chitosan-grafted polycaprolactone nanofibrous membranes. *Acta Biomater.* **10**, 4971–4982 (2014).
46. O. R. Ozerdem, R. Anlatici, T. Bahar, F. Kayaselcuk, O. Barutcu, I. Tuncer, O. Sen, Roles of periosteum, dura, and adjacent bone on healing of cranial osteonecrosis. *J. Craniofac. Surg.* **14**, 371–379 (2003).
47. A. K. Gosain, T. D. Santoro, L. S. Song, C. C. Capel, P. V. Sudhakar, H. S. Matloub, Osteogenesis in calvarial defects: Contribution of the dura, the pericranium, and the surrounding bone in adult versus infant animals. *Plast. Reconstr. Surg.* **112**, 515–527 (2003).
48. S. Chen, J. V. John, A. McCarthy, M. A. Carlson, X. Li, J. Xie, Fast transformation of 2D nanofiber membranes into pre-molded 3D scaffolds with biomimetic and oriented porous structure for biomedical applications. *Appl. Phys. Rev.* **7**, 021406 (2020).
49. A. McCarthy, L. Saldana, D. McGoldrick, J. V. John, M. Kuss, S. Chen, B. Duan, M. A. Carlson, J. Xie, Large-scale synthesis of compressible and re-expandable three-dimensional nanofiber matrices. *Nano Select.* **2021**, 1–14 (2021).
50. S. Chen, H. Wang, Y. Su, J. V. John, A. McCarthy, S. L. Wong, J. Xie, Mesenchymal stem cell-laden, personalized 3D scaffolds with controlled structure and fiber alignment promote diabetic wound healing. *Acta Biomater.* **108**, 153–167 (2020).

Acknowledgments
Funding: This work was supported by grants from the National Institute of General Medical Science (NIGMS) at the NIH (R01GM123081, R01GM138552, and P30GM127200), National Institute of Dental and Craniofacial Research (NIDCR) at the NIH (1R21DE027516), Congressionally Directed Medical Research Program (CDMRP)/Peer Reviewed Medical Research Program (PRMRP) FY19 W81XWH2010207, NE LB606, and startup funds from the University of Nebraska Medical Center (UNMC). Collagen SHG imaging and analyses were conducted by H. J. Smith at the Multiphoton Intravital and Tissue Imaging Core (UNMC), which receives support through the Nebraska Center for Nanomedicine (NCN) Center for Biomedical Research Excellence (Institutional Development Award, NIGMS of the NIH, P30GM127200), state funds from the Nebraska Research Initiative, and institutionally by the UNMC Office of the Vice Chancellor for Research. **Author contributions:** S.C. and J.X. conceived the study idea. S.C., J.X., and H.W. designed the experiments. S.C., H.W., V.L.M., and G.T. performed the experiments and computational simulation. All authors contributed to writing the manuscript, discussing the results, and implications and editing the manuscript at all stages. **Competing interests:** The authors declare that they have no competing interests. **Data and materials availability:** All data needed to evaluate the conclusions in the paper are present in the paper and/or the Supplementary Materials. Additional data related to this paper may be requested from the authors.

Submitted 23 December 2020
Accepted 11 June 2021
Published 28 July 2021
10.1126/sciadv.abg3089

Citation: S. Chen, H. Wang, V. L. Mainardi, G. Talò, A. McCarthy, J. V. John, M. J. Teusink, L. Hong, J. Xie, Biomaterials with structural hierarchy and controlled 3D nanotopography guide endogenous bone regeneration. *Sci. Adv.* **7**, eabg3089 (2021).